

Materials Advances

Accepted Manuscript

This article can be cited before page numbers have been issued, to do this please use: A. Ben Abdelhadi, S. Hidaoui, R. Ouarsal, M. Poupon, M. Dušek, M. L. Palop, M. A. López de la Torre, L. Lezama, B. El Bali, M. Lachkar and A. Douhal, *Mater. Adv.*, 2026, DOI: 10.1039/D5MA01055A.



This is an Accepted Manuscript, which has been through the Royal Society of Chemistry peer review process and has been accepted for publication.

Accepted Manuscripts are published online shortly after acceptance, before technical editing, formatting and proof reading. Using this free service, authors can make their results available to the community, in citable form, before we publish the edited article. We will replace this Accepted Manuscript with the edited and formatted Advance Article as soon as it is available.

You can find more information about Accepted Manuscripts in the [Information for Authors](#).

Please note that technical editing may introduce minor changes to the text and/or graphics, which may alter content. The journal's standard [Terms & Conditions](#) and the [Ethical guidelines](#) still apply. In no event shall the Royal Society of Chemistry be held responsible for any errors or omissions in this Accepted Manuscript or any consequences arising from the use of any information it contains.

A novel copper formate-based framework $\text{RbCu}(\text{HCO}_2)_2\text{Cl}$: synthesis, crystal structure, thermal, vibrational and magnetic properties and antibacterial activity

View Article Online
DOI: 10.1039/D5MA01055A

Asmae Ben Abdelhadi,^{a,b} Safaa Hidaoui,^a Rachid Ouarsal,^a Morgane Poupon,^c Michal Dusek,^c María de los Llanos Palop Herreros,^d Marco Antonio López de la Torre,^e Luis Lezama,^f Brahim El Bali,^a Mohammed Lachkar*,^a and Abderrazzak Douhal*,^b

^aEngineering Laboratory of Organometallic, Molecular Materials, and Environment (LIMOME), Faculty of Sciences, Sidi Mohamed Ben Abdellah University, 30000 Fez, Morocco.

^bDepartamento de Química Física, Facultad de Ciencias Ambientales y Bioquímica, e INAMOL, Campus Tecnológico de Toledo, Universidad de Castilla-La Mancha (UCLM), Avenida Carlos III, S.N., 45071 Toledo, Spain.

^cInstitute of Physics of the Czech Academy of Sciences, Na Slovance 2, 8, Praha 182 21, Czech Republic.

^dDepartamento de Química Analítica y Tecnología de los Alimentos, Facultad de Ciencias Ambientales y Bioquímica, Universidad de Castilla-La Mancha, (UCLM), Avenida Carlos III, S.N., 45071 Toledo, Spain.

^eDepartamento de Física, Facultad de Ciencias Ambientales y Bioquímica, y INAMOL, Universidad de Castilla-La Mancha, Avenida Carlos III, S.N., 45071 Toledo, Spain.

^fDepartamento de Química Orgánica e Inorgánica, Facultad de Ciencia y Tecnología, Universidad del País Vasco, UPV/EHU, Bº Sarriena s/n, 48940 Leioa, Spain.

*Corresponding authors: mohammed.lachkar@usmba.ac.ma (M. L.) & Abderrazzak.Douhal@uclm.es (A. D.)



Abstract

View Article Online
DOI: 10.1039/D5MA01055A

In this contribution, we report on the synthesis and characterization of a novel biologically active Cu(II)-based paddlewheel (PW) metal–organic framework (MOF), $\text{RbCu}(\text{HCO}_2)_2\text{Cl}$ (**1**). Single-crystal X-ray diffraction result confirmed a monoclinic unit cell with space group $P2_1/n$ and the Rb^+ cation as a counter-balanced ion located in the cavities of the framework of the dinuclear copper-copper dimer formed by a PW-arrangement of formate anions in the *syn-syn* configuration. Each Cu(II) atom has a square pyramidal environment with a $\text{Cu}\cdots\text{Cu}$ intramolecular distance of 2.7070 (7) Å. The IR spectrum confirms the existence of the formate anion (HCO_2^-). Magnetic susceptibility experiments, performed from 5 to 300 K, revealed a strong antiferromagnetic coupling ($J = -531 \text{ cm}^{-1}$) between the two Cu^{2+} ions linked by four formate groups. The powder EPR spectra show the typical lines of the triplet state ($S = 1$) with significant zero-field splitting, attributed to $\text{Cu}^{2+}\text{--Cu}^{2+}$ dimers. *In vitro* antibacterial activity was evaluated against two Gram-positive bacteria (*Staphylococcus aureus* CECT 86 and *Listeria monocytogenes* CECT 4031) and two Gram-negative bacteria (*Escherichia coli* CECT 99 and *Klebsiella pneumoniae* CECT 143^T). The studies revealed that MOF **1** exhibits both bacteriostatic and bactericidal activity against all the microorganisms analyzed, making it a potential candidate for treating bacterial infections. The obtained findings give more insight into the interesting properties of Cu-based frameworks and antibacterial activity.

Keywords: Cu formate-based MOF· Dinuclear Cu(II) paddle-wheel· Crystal structure· Vibrational studies· EPR· Magnetic properties· Antibacterial activity.



1. Introduction

View Article Online
DOI: 10.1039/D5MA01055A

Metal–organic frameworks (MOFs) are an important class of hybrid crystalline materials made of metal centres and organic linkers. They offer adjustable structures, high porosity, and multifunctionality. Their structural flexibility and chemical diversity have enabled many applications, including catalysis, gas storage, sensing, magnetism and increasingly, biological uses.^{1–4} Recently research has focused on exploring MOFs with binuclear paddle wheel (PW) topology. Their outstanding porosity, adjustable design and their unique physicochemical properties make them promising for various applications, such as biologically active agents, electrochemical processes, ferroelectric and dielectric materials, magnetism, catalysis, supramolecular assemblies, and molecular magnetic devices.^{14–18} Among various metal ions used in PW-based MOF chemistry, copper is one of the most widely employed metal centres for forming paddle-wheel structures, it is a significant transition metal in biology and coordination chemistry.^{19–23} Copper is an essential trace element in the human body. In addition, it plays crucial roles in many biological processes and enzyme regulation, as well as in the structural and functional enhancement of proteins. It exhibits intrinsic antimicrobial and redox activity. Consequently, the combination of biologically relevant copper centres with the structural robustness of the PW motif offers a promising platform for the design of functional materials with enhanced biological activity.^{24, 25} Notably, numerous studies have shown that Cu–PW MOFs have been extensively explored for biological applications, including antibacterial, anticancer, antifungal, antimicrobial, and antiviral activities, which arise from the unique coordination sphere around central Cu(II) cations, their ability to catalyze the generation of reactive oxygen species (ROS), disrupt membrane integrity, interact with nucleic acids, and inhibit key microbial enzymes.^{24, 26, 27} These multifunctional properties make Cu(II) MOFs biologically more relevant and functional than the other compounds. The higher biological activity of Cu(II)-based MOFs is significantly influenced by the nature of the ligands used. In particular, N- and O-donor ligands represent a promising class of candidates in the development of new Cu(II)-based antimicrobial materials. These ligands often coordinate the copper metal through different coordination geometries (four, five, or six), forming a stable chelating framework. This chelation process generally reduces the polarity of the copper center, increases the lipophilicity of the compound and thereby improves its ability to penetrate biological membranes, leading to



enhanced biological activity.^{26, 28-30} In addition, Cu PW-based MOFs have gained significant interest, owing to their magnetic behaviour, facilitated by the rather short formate anion HCO_2^- , which allows strong magnetic coupling between the Cu(II) centers.^{35, 36} In general, Cu(II)-based compound contains an unpaired d^9 electron configuration which gives it paramagnetic properties. Additionally, it has been reported that the coupling of the d^9 unpaired electrons between the Cu(II) centers can result in a triplet (high spin) or a singlet (low spin) ground state or other magnetic properties such as ferromagnetic (FM) and antiferromagnetic (AFM) behavior, respectively, depending on the types of coordination modes, metal geometry and environment.^{37, 38} In this context, the design and development of novel Cu-based PW frameworks, along with the investigation of their magnetic behaviour and the exploration of their biological activity, remains an active and promising research for a better understanding of the structure-activity relationship.

Herein, we synthesized, fully characterized, examined the magnetic properties examined the magnetic properties, and explored the biological activity of a novel Cu(II)-based metal-formate framework $\text{RbCu}(\text{HCO}_2)_2\text{Cl}$ (**1**), containing the largest possible monoatomic A-site cations Rb^+ . Cu-based MOF was obtained by a slow diffusion method, with excellent reproducibility and was fully characterized by a combination of a single crystal X-ray diffraction (SXRD), thermal stability, EPR and SQUID measurements. At 300 K, compound **1** crystallizes in the monoclinic system with space group $P2_1/n$, and its crystal structure features the well-known paddle-wheel motif typical of copper formates, $\text{Cu}_2(\text{HCOO})_4$, with an intramolecular Cu...Cu distance of 2.7070(7) Å within the dinuclear unit. Magnetic susceptibility data, obtained from 5 to 300 K, revealed that sample **1** exhibits a strong antiferromagnetic coupling ($J = -531 \text{ cm}^{-1}$) between the two Cu^{2+} ions linked by four formate groups, which form the Cu_2 paddle-wheel units that give rise to the anionic network in this compound. Furthermore, we also evaluated the *in vitro* antibacterial activity of MOF **1** against two Gram-positive bacteria, *S. aureus* CECT 86 and *L. monocytogenes* CECT 4031, and two Gram-negative bacteria, *E. coli* CECT 99 and *K. pneumoniae* CECT 143^T, using both the disc diffusion and the agar well diffusion method.

2. Experimental Section

2.1. Materials



All the chemicals are reagent grade and were used as supplied. Copper (II) chloride tetrahydrate ($\text{CuCl}_2 \cdot 4\text{H}_2\text{O}$, 99.9 %) and formic acid (HCOOH , 98 %) were purchased from Fluka (Switzerland). Rubidium carbonate (Rb_2CO_3 , 99.5 %) was bought from Sigma-Aldrich (France) and anhydrous methanol (99.7 %) was purchased from Panreac (Spain).

2.2. Synthesis

The green prismatic single crystals of compound **1** were obtained using a mild solution chemistry approach at ambient temperature using methanol as solvent, since it is widely known as a non-coordinating solvent in synthesizing metal formate frameworks.⁴⁴ In a typical synthesis procedure, 10 mL of a methanolic solution containing 4 mmol Rubidium carbonate (0.92 g) and 80 mmol formic acid (4 mL) were placed at the bottom of a glass tube. Upon this solution, 10 mL of a methanolic solution containing 2 mmol of $\text{CuCl}_2 \cdot 4\text{H}_2\text{O}$ (0.340 g) were carefully layered on top. The tube was sealed and undisturbed at room temperature for several days until green square-shaped crystals formed. The crystals of **1** were subsequently isolated by filtration, washed three times with ethanol, and dried at room temperature for 24h, are quite stable (Figure S1). HR-ESI-MS (negative mode) m/z calculated for $\text{RbCuC}_2\text{H}_2\text{O}_4\text{Cl}$: 274.50100; found: 273.94864.

2.3. Characterizations and Measurements

Single-crystal data sets were collected at 300 K, on a suitable green single crystal of compound **1** with dimensions $0.36 \times 0.30 \times 0.27 \text{ mm}^3$. Data collection was performed using Mo $K\alpha$ radiation ($\lambda = 0.71073 \text{ \AA}$) from a classical sealed tube monochromated by graphite and collimated by fibre-optics enhanced collimator. As a detector, we used a CCD Atlas S2. CrysAlis PRO software (CrysAlis PRO 1.171.41.117a, Rigaku Oxford Diffraction, 2021) was used to process the data and an empirical multiscan absorption correction was applied using spherical harmonics, implemented in the SCALE3 ABSPACK scaling algorithm. The structure was solved by charge flipping with the program SUPERFLIP package⁴⁵ and refined against F^2 by using full-matrix least-squares methods with the Jana2020 program package.⁴⁶ All non-hydrogen atoms were refined with anisotropic thermal displacement parameters. For all the hydrogen atoms, we kept $U_{\text{iso}}(\text{H})$ equal to $1.2U_{\text{eq}}(\text{C/N})$. Visualization of the structure was made using the Diamond program.⁴⁷



The details concerning the crystal data, data collection, and refinement are given in

View Article Online
DOI: 10.1039/D5MA01055A

Table 1. At the same time, the refined atomic positions and displacement parameters are listed in Tables S1 and S2, respectively. The data can be obtained free of charge from the Cambridge Crystallographic Data Centre (CCDC) via www.ccdc.cam.ac.uk/data_request/cif (CCDC **2468965**).

Table 1. Crystal data and structure refinement parameters of $\text{RbCu}(\text{HCO}_2)_2\text{Cl}$.

Crystal data	
Chemical formula	$\text{C}_2\text{H}_2\text{ClCuO}_4\text{Rb}$
M_r (g/mol)	274.5
Crystal system, space group	Monoclinic, $P2_1/n$
Temperature (K)	300
a, b, c (Å)	8.242 (2), 7.979 (2), 9.723 (2)
β (°)	95.40 (3)
V (Å ³)	636.5 (3)
Z	4
Radiation type	Mo $K\alpha$
μ (mm ⁻¹)	11.38
Data collection	
Diffractometer	Xcalibur, AtlasS2, Gemini ultra
T_{\min}, T_{\max}	0.575, 1
No. of measured, independent and observed [$I > 3\sigma(I)$] reflections	9955, 1645, 1329
R_{int}	0.041
$(\sin \theta/\lambda)_{\max}$ (Å ⁻¹)	0.691
Refinement	
$R[F^2 > 2\sigma(F^2)], wR(F^2), S$	0.023, 0.058, 1.30
No. of reflections	1645
No. of parameters	83
H-atom treatment	H-atom parameters constrained
$\Delta\rho_{\max}, \Delta\rho_{\min}$ (e Å ⁻³)	0.46, -0.54

Mass spectrometry (MS) analyses. MS analyses were performed using a high-resolution Exactive Plus Orbitrap mass spectrometer (Thermo Scientific) equipped with an electrospray ionization (ESI) source.



Infrared Spectroscopy Measurements. The room-temperature IR (Infrared) spectrum in the mid-IR ($4000\text{--}400\text{ cm}^{-1}$) range has been measured with Vertex 70 (Bruker) Fourier transform infrared spectrometer (FTIR) using the attenuated total reflectance (ATR) method. The spectral resolution was 4 cm^{-1} .

Thermogravimetric Analysis (TGA) and Differential Thermal Analysis (DTA). TGA-DTA analysis for the investigated compound was performed in the temperature range of 315 to 560 K using the « LINSEIS TGA PT1600 ». The sample weight was 3 mg. The heating speed rate was 10 K/min using an open platinum crucible under airflow.

EPR and Magnetometry Measurements. X-band EPR measurements were carried out on a Bruker ELEXSYS 500 spectrometer equipped with a super-high-Q resonator ER-4123-SHQ and a maximum available microwave power of 200 mW. Powder samples were placed in quartz tubes and spectra were recorded at different temperatures between 4 and 300 K using standard Oxford Instruments low-temperature devices. The magnetic field was calibrated with an NMR probe and the frequency inside the cavity ($\sim 9.4\text{ GHz}$) was determined with an integrated MW-frequency counter. For Q-band studies, EPR spectra were recorded at room temperature on a Bruker EMX system equipped with an ER-510-QT resonator. The frequency inside the cavity ($\sim 34\text{ GHz}$) was determined with a Hewlett-Packard 5352B microwave frequency counter. Data were collected and processed using the Bruker Xepr suite. Temperature-dependent magnetic susceptibility measurements were performed between 5 and 300 K with an applied field of 1 kOe, using a MPMS3 SQUID magnetometer (Quantum Design). Magnetization of powdered samples was measured at temperatures of 5 and 300 K with magnetic fields ranging from 70 to 70 kOe. The experimental data were corrected for diamagnetism of the constituent atoms, by using Pascal tables, and the sample holder.

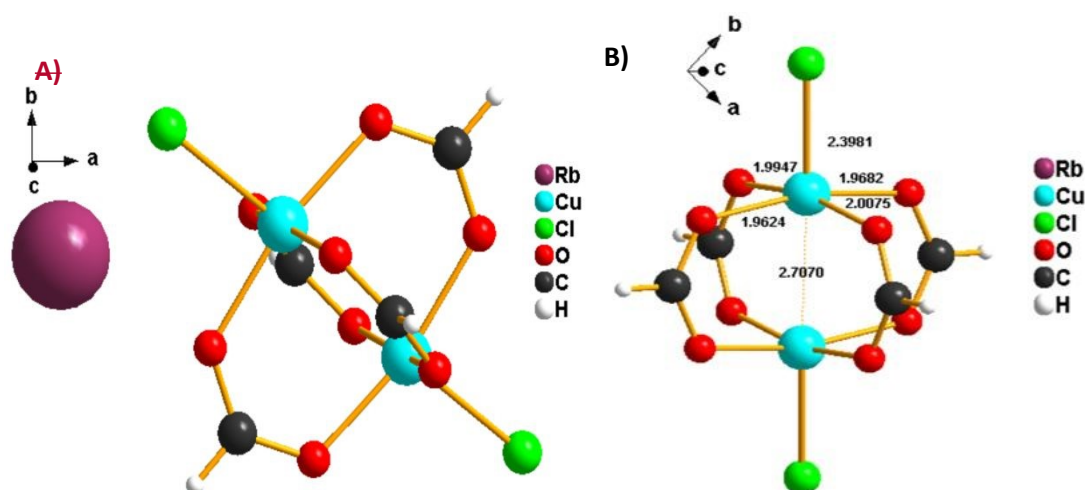
3. Results and Discussion

3.1. Crystal Structure

The green single crystals of $\text{RbCu}(\text{HCO}_2)_2\text{Cl}$ were prepared by a facile slow diffusion solution process at room temperature. Single crystal X-ray diffraction (SCXRD) studies reveal that the compound crystallizes in a monoclinic system with space group $P2_1/n$, $a = 8.242(2)\text{ \AA}$, $b = 7.979(2)\text{ \AA}$, $c = 9.723(2)\text{ \AA}$, $\beta = 95.40(3)^\circ$ and $V = 636.5(3)\text{ \AA}^3$ at 300.1 K. Compound **1** shows a



well-known paddle-wheel structure typical for copper formates (Figure 1A). The asymmetric unit of compound **1** contains one alkali metal (Rb^+) and a binuclear copper (II) paddle-wheel (PW), which contains two Cu^{2+} ions *syn-syn* connected via four oxygen atoms from four different formate groups $\text{Cu}_2(\text{HCOO})_4$. Each Cu(II) atom is also coordinated with a disordered chloride ion in the apical position, contributing to the framework's charge-neutrality. The result is a slightly distorted CuO_4Cl square pyramidal environment around each Cu(II) with a $\text{Cu} \cdots \text{Cu}$ intramolecular distance of 2.7070 (7) Å in the binuclear unit (Figure 1B), as described for the isostructural $\text{CsCu}(\text{HCOO})_2\text{Cl}^{50}$ and close to that of other compounds with similar structures.^{22, 35, 36} In these square pyramidal geometries, the copper ions Cu(II) lie above the basal plane towards the apical chloride ions. In addition, the planes of basal bonds around the copper ions are parallel to one another (Figure 1C). This typical structure represents the simplest paddle-wheel geometry possible, its widely known copper formate.^{25, 51}



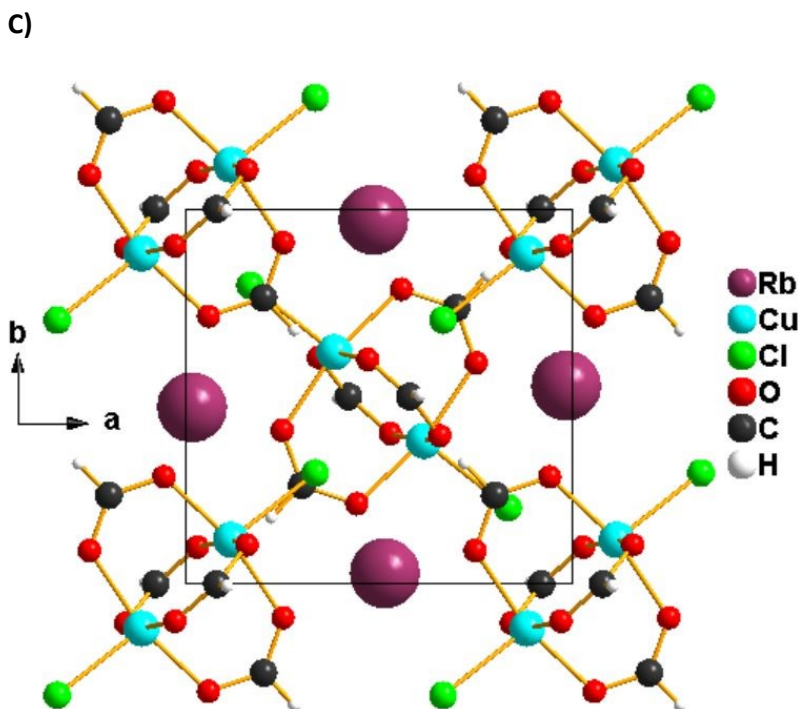


Figure 1. A) Molecular structure of $\text{RbCu}(\text{HCO}_2)_2\text{Cl}$. B) Selected bond lengths (unit: Å) of Cu in the dinuclear (PW) copper(II) moieties. C) Three-dimensional view of the crystal structure of compound **1** illustrates the local coordination of Cu in the dinuclear (PW) copper(II) moieties.

The values of bond distances (Å) and bond angles (°) are shown in Table 2. The $\text{Cu}-\text{O}_{\text{formate}}$ bond lengths range from 1.9624 (2) to 2.0075 (2) Å (Figure 1B and Table 2). The apical bond distance $\text{Cu}-\text{Cl}$ is 2.3981 (12) Å. These bond length values agree with bond distances for other binuclear $\text{Cu}(\text{II})$ compounds.^{23, 38, 50, 52} The bond angles $\text{Cl}_{(\text{eq})}-\text{Cu}-\text{O}_{\text{formate}}$ range from 92.30 (7) to 101.42 (7) ° (Table 2). The formate moieties have rather common bond angles, 126.9 (3) ° for $\text{O}_2-\text{C}_1-\text{O}_3^{\text{iii}}$ and 127.5 (3) ° for $\text{O}_1-\text{C}_2-\text{O}_4^{\text{vi}}$ (Table 2). The bond angle for the moiety $\text{Cl}_1-\text{Cu}_2-\text{Cu}_2$ is 168.943 (6) °, showing a small deviation from linearity along the $\text{Cu}-\text{Cu}$ axis.

Table 2. Geometric parameters (Å, °) for $\text{RbCu}(\text{HCO}_2)_2\text{Cl}$.

Cu_2-Cl_1	2.3981 (12)	Cu_2-O_2	1.962 (2)
$\text{Cu}_2-\text{O}_1^{\text{i}}$	2.008 (2)	Cu_2-O_3	1.968 (2)
O_1-C_2	1.245 (4)	Cu_2-O_4	1.995 (2)
O_2-C_1	1.255 (4)	$\text{O}_3-\text{C}_1^{\text{iii}}$	1.255 (4)
$\text{C}_1-\text{H}_{1\text{c}1}$	0.96	$\text{O}_4-\text{C}_2^{\text{iv}}$	1.253 (4)
$\text{C}_2-\text{H}_{1\text{c}2}$	0.96	$\text{Cl}_1-\text{Cu}_2-\text{O}_2$	101.42 (7)
$\text{Cl}_1-\text{Cu}_2-\text{O}_1^{\text{i}}$	92.35 (7)	$\text{Cl}_1-\text{Cu}_2-\text{O}_3$	92.30 (7)
$\text{Cl}_1-\text{Cu}_2-\text{O}_4$	101.29 (7)	$\text{Cu}_2-\text{O}_2-\text{C}_1$	119.3 (2)
$\text{O}_1^{\text{i}}-\text{Cu}_2-\text{O}_2$	88.58 (9)	$\text{Cu}_2-\text{O}_3-\text{C}_1^{\text{iii}}$	127.2 (2)



O1 ⁱ —Cu2—O3	91.45 (9)	Cu2—O4—C2 ^{iv}	119.4 (2)	View Article Online DOI: 10.1039/D5MA01055A
O1 ⁱ —Cu2—O4	166.34 (9)	O2—C1—O3 ⁱⁱⁱ	126.9 (3)	
O2—Cu2—O3	166.26 (10)	O2—C1—H1c1	116.54	
O2—Cu2—O4	88.07 (9)	O3 ⁱⁱⁱ —C1—H1c1	116.54	
O3—Cu2—O4	88.69 (9)	O1—C2—O4 ^{vi}	127.5 (3)	
O1—C2—H1c2	116.23	O4 ^{vi} —C2—H1c2	116.23	
Cu2 ⁱ —O1—C2	126.3 (2)			

Symmetry codes : (i) $-x, -y+1, -z+1$; (ii) $x-1/2, -y+3/2, z-1/2$; (iii) $-x+1, -y+1, -z+1$; (iv) $x+1, y, z$;
(v) $x+1/2, -y+3/2, z+1/2$; (vi) $x-1, y, z$.

In a unit cell, besides the two binuclear Paddle Wheel (PW) copper (II) moieties, there are four Rb⁺ cations located in the empty spaces within the three-dimensional framework formed by the binuclear Paddle Wheel (PW) copper(II) units (Figure 2). The dinuclear PW units together with the Rb⁺ cations form a herringbone arrangement when viewed down the a -axis. The Rb⁺ cations, which are responsible for the charge balance of the Cu-based compound as counter ions, are bonded to four binuclear paddle wheel Cu₂(HCOO[−])₄ dimers via formate oxygen and chloride anions through Rb–O and Rb–Cl electrostatic interactions, resulting in an extended three-dimensional coordination framework. These coordination linkages connect adjacent paddle-wheel units into zigzag infinite chains parallel to the a -axis, thereby reinforcing the overall structural stability of the network. The overall supramolecular arrangement, dominated by electrostatic interactions, is comparable to that of CsCu(HCOO)₂Cl.⁵⁰ In contrast, in the [NH₃(CH₂)₂NH₃][Cu₂(HCOO)₄Cl₂] metal-organic compounds ($n = 3, 4$), structural stability is primarily ensured by N–H⁺⋯O and N–H⁺⋯Cl[−] hydrogen-bond interactions.⁵³



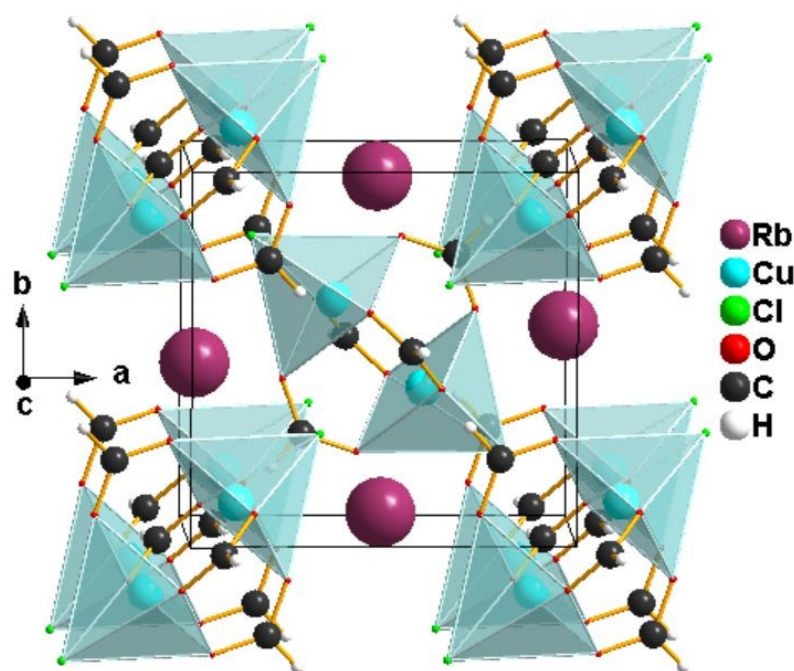


Figure 2. Polyhedral presentation of the coordination environments of the Cu in $\text{RbCu}(\text{HCO}_2)_2\text{Cl}$. The 3D-framework cavities, formed by the dinuclear Paddle Wheel (PW) copper (II) units, are occupied by Rb^+ cations.

3.2. Vibrational Properties

Figure 3 exhibits room-temperature IR spectrum of $\text{RbCu}(\text{HCO}_2)_2\text{Cl}$, while Table S3 exhibits the values of IR absorption band frequencies and their assignment. The IR spectrum of the Cu(II)-based compound exhibits all the strongest characteristic formate vibration bands. It is well known that the formic HCO_2^- ions consist of six internal modes: The C-H stretching mode ν_1 , the symmetric C-O stretching mode ν_2 , the antisymmetric C-O stretching mode ν_4 , the symmetric O-C-O bending (scissor) mode ν_3 , the C-H in-plane bending mode ν_5 , and the C-H out-of-plane bending mode ν_6 .^{54, 55} These modes were observed in narrow wavenumber ranges for different metal formate frameworks.^{56, 57} In the high wavenumber region besides the $\nu_1(\text{HCO}_2)$ modes, others expected bands attributed to some combinations and overtones of other $\nu(\text{HCO}_2)$ modes can be observed. From Figure 3, the vibrations bands at 2895 and 2845 cm^{-1} are assigned to the stretching mode $\nu_1(\text{HCO}_2)$, while the IR spectrum shows two very weak vibrations bands at 2976 and 2945 cm^{-1} are related to the combination of $\nu_4(\text{HCO}_2)$ and $\nu_5(\text{HCO}_2)$ modes, and the overtones $2\nu_5$ and $2\nu_2$, respectively. The strong bands observed at 1614 and 1552 cm^{-1} in the medium wavenumber region, could belong to $\nu_4(\text{HCOO})$



asymmetric C–O stretching modes of the CO_2^- moiety. The C–H in-plane bending mode ν_5 (HCO_2^-) are observed as medium IR bands in the region $1413\text{--}1376\text{ cm}^{-1}$. Additionally, the intense vibration band located at 1337 cm^{-1} is assignable to the symmetric C–O stretching mode $\nu_2(\text{HCO}_2^-)$. In the spectrum, a significant shift in the $\nu(\text{C–O})$ and $\nu(\text{C=O})$ stretching can be observed in reference to the spectra of free formate ions (HCO_2^-), confirming the coordination of the copper Cu(II) to the formate groups. The modes observed in the lower wavenumber region at 1045 and 769 cm^{-1} are assigned as the out-of-plane C–H bending mode $\nu_6(\text{HCO}_2^-)$ and the symmetric O–C–O bending mode $\nu_3(\text{HCO}_2^-)$, respectively. Finally, the strong vibration band observed at 403 cm^{-1} is due to Cu–O bonds. These results agree well with those reported for other Cu-based formate frameworks.^{13, 58, 59}

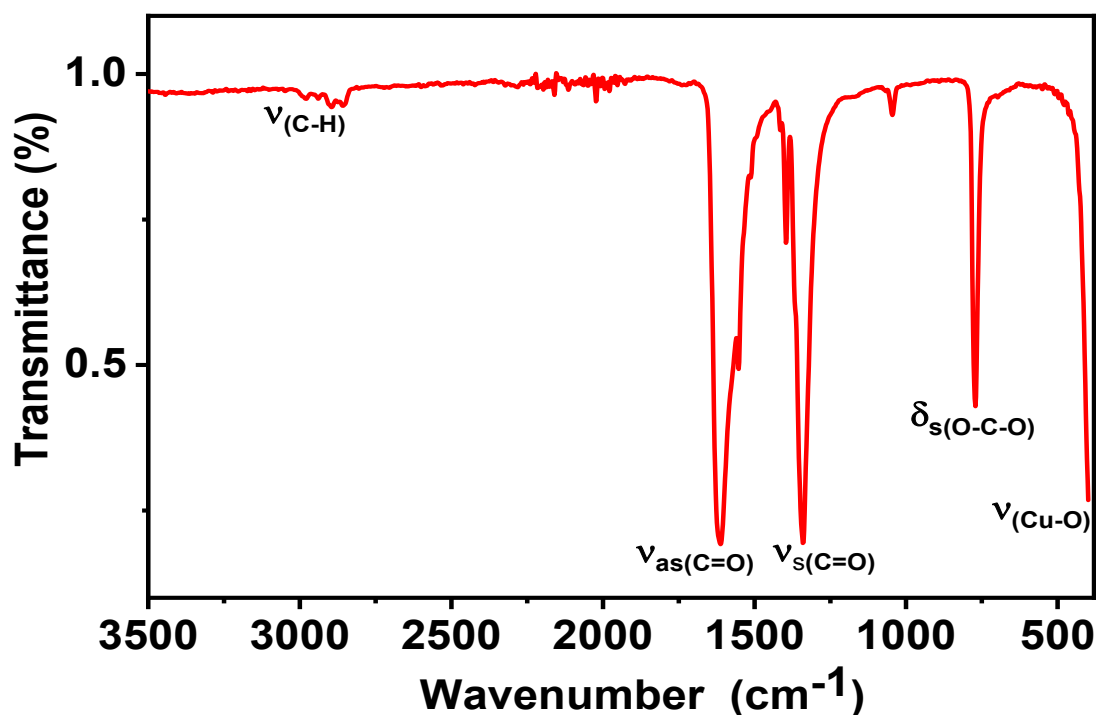


Figure 3. Room-temperature IR spectrum of $\text{RbCu}(\text{HCO}_2)_2\text{Cl}$.

3.4. Thermal Properties

The thermal stability of $\text{RbCu}(\text{HCO}_2)_2\text{Cl}$ was investigated using combined thermogravimetric analysis (TGA) and differential thermal analysis (DTA) on a crystalline



powder sample in an air atmosphere at a heating rate of 10 K/min, from 315 to 780 K (Figure 4). TGA results reveal that compound **1** is thermally stable up to 350 K, and above this temperature, it begins to decompose in one main mass loss step, as observed in the TGA curve (red curve in Figure 4). The experimental percent weight loss is approximately 31.67%, which is close to the expected (calculated) loss of two formate ligands per formula unit (theoretical value: 32.78%). This decomposition is found to be exothermic, as indicated by the DTA, which displays an exothermic peak at 426 K (green curve in Figure 4). This result is similar to the one reported for $\text{CsCu}(\text{HCO}_2)_2\text{Cl}$, in which the degradation occurs in one main weightless step at approximately 425 K.⁵⁰ During the whole decomposition process of compound **1**, the resulting residue formed corresponds to binary (RbCl) and metallic Cu species. These results align well with the observed thermal behavior of other Cu-containing formate-based alkali metals, where decomposition occurs over very small temperature intervals and at low onset temperatures.^{59, 60} Additionally, a small mass degradation is observed in the TGA curve at higher temperatures, which could be attributed to internal redox reactions where copper is reduced. Subsequently, the residue remains nearly stable up to 500 K.

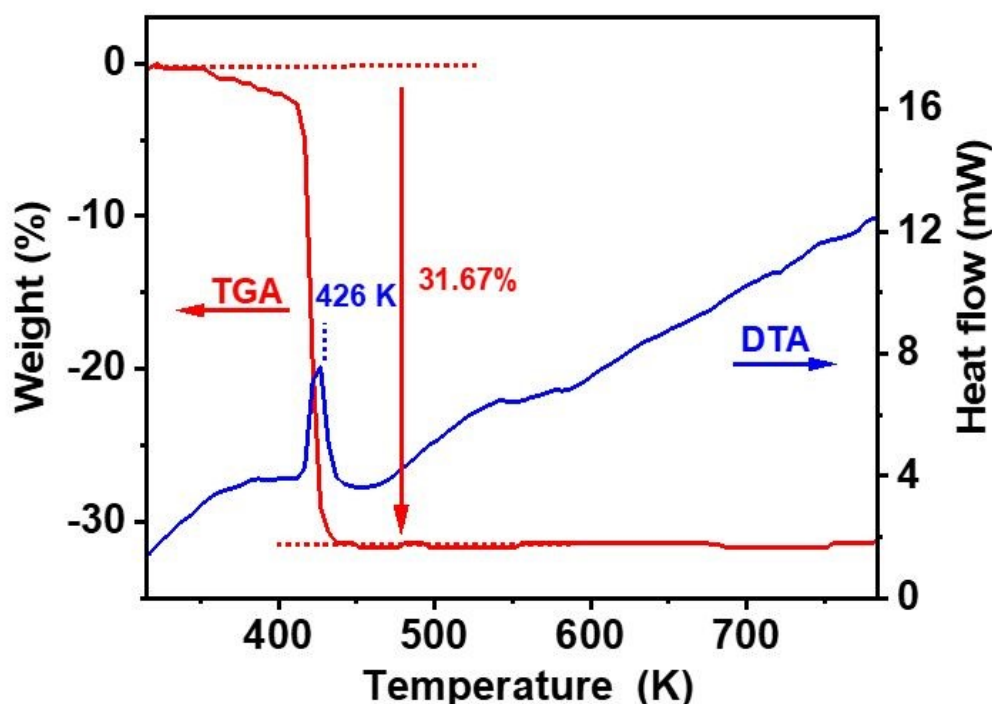


Figure 4. Combined TGA-DTA curves for $\text{RbCu}(\text{HCO}_2)_2\text{Cl}$.



3.5. Magnetic Properties

View Article Online
DOI: 10.1039/D5MA01055A

Variable temperature magnetic susceptibility measurements were performed on powdered samples of $\text{RbCu}(\text{HCO}_2)_2\text{Cl}$ in the temperature range 5–300 K. Plots of the thermal evolution of the magnetic molar susceptibility (χ_m) and the $\chi_m T$ product ($\chi_m T = \mu_{\text{eff}}^2/8$) are shown in Figure 5. At room temperature, $\chi_m T$ is equal to $0.11 \text{ cm}^3\text{K/mol}$ ($\mu_{\text{eff}} = 0.94 \mu_B$), a value significantly lower than the theoretical spin-only value for a $S=1/2$ system ($0.375 \text{ cm}^3\text{K/mol}$). Upon cooling, $\chi_m T$ continuously decreases, and it practically vanishes at low temperatures ($\chi_m T = 0.002 \text{ cm}^3\text{K/mol}$ at 5 K). The susceptibility decreases from 300 to 80 K and rapidly increases as the temperature is lowered further to 5 K, probably due to the small amount of paramagnetic Cu(II) compound detected in the EPR study. This behavior is consistent with a strong antiferromagnetic coupling between the two Cu^{2+} ions linked by four formate groups which form the Cu_2 paddle-wheel units that give rise to the anionic network in this compound. Therefore, we tried to fit the susceptibility data using the Bleaney-Bowers equation for a Cu(II) dimer⁶¹ (equation (1)) combined with an additional term accounting for a paramagnetic contribution, assumed to come from a species with the same molecular weight per Cu(II) ion and g-value as the main compound to avoid overparameterization.⁶²

$$\chi_m = (1 - \delta) \frac{Ng^2\beta^2}{kT} \frac{1}{3 + \exp(-J/kT)} + \delta \frac{Ng^2\beta^2}{4kT} \quad (1)$$

where J is the singlet–triplet energy gap, defined by the spin Hamiltonian $H = -JS_1 \cdot S_2$ ($S_1 = S_2 = 1/2$), g is the Lande's g factor and p is the percent of noncoupled impurity; N , β , and k are the Avogadro's number, the Bohr magneton, and Boltzmann's constant, respectively. The best-fit parameters obtained by minimizing the reliability R factor, $R = \sum [(\chi_m T)_{\text{exp}} - (\chi_m T)_{\text{cal}}]^2 / \sum [(\chi_m T)_{\text{exp}}]^2$, are $J = -531 \text{ cm}^{-1}$, $g = 2.125$ and $\delta = 0.0047$, with $R = 2.8 \times 10^{-5}$. As shown in Figure 5, the calculated curves reproduce the magnetic data very well over the whole temperature range investigated. The obtained singlet-triplet energy gap is close to the average value ($J = -550 \text{ cm}^{-1}$) determined for copper carboxylate complexes with the same core, although it is somewhat larger than that calculated ($J = -425 \text{ cm}^{-1}$) for a model compound $[\text{Cu}_2(\mu\text{-HCOO})_4(\text{H}_2\text{O})_2]$ with an intradimeric Cu–Cu distance of 2.707 \AA .⁶³ This is due to the presence of chloride ions as axial ligands and to slight differences in the geometry of the carboxylate bridges arising from the Rb–Cl and Rb–O bonds, which stabilize the three-dimensional framework. Despite the short Cu–Cu distance, super exchange is the dominant



coupling mechanism in Cu dimers with *syn-syn* coordination mode of the formate groups because the unpaired electron on each copper(II) ion occupies parallel $d_{x^2-y^2}$ orbitals oriented towards the oxygen atoms of the bridging ligands. Therefore, the coupling constant can be strongly affected by small structural changes in this type of compound.

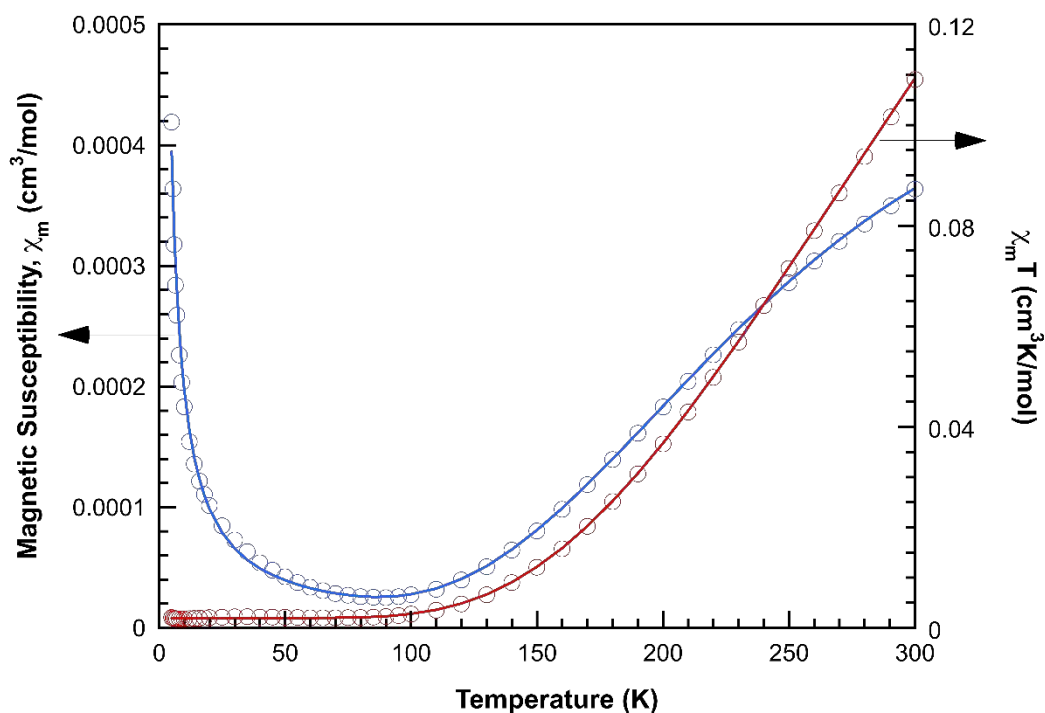


Figure 5. Magnetic behavior of compound $\text{RbCu}(\text{HCO}_2)_2\text{Cl}$. The solid lines represent the best least-squares fit to experimental data (see text for details of fit).

Notably, this compound does not exhibit the complex magnetic behavior observed by Zhou *et al.* for the isostructural $\text{CsCu}(\text{HCOO})_2\text{Cl}$ material.⁵⁰ The susceptibility curves recorded on zero-field cooled (ZFC) and field cooled (FC) samples show no signs of irreversibility above 5 K. Furthermore, there is no indication of a magnetic transition, such as those observed at 8 and 32 K in the aforementioned compound. At room temperature, the field-dependent magnetization displays a straight line as expected for a classic paramagnetic compound (not shown). A small ferromagnetic anomaly can be detected in the magnetization measurements at 5 K, but it is practically negligible (see Figure S3). In fact, the magnetization curve at 5 K can be reasonably well described by the Brillouin function for a system with $S=1/2$ normalized to account for the percentage of paramagnetic impurity deduced from the susceptibility fit.⁶⁴



Considering the strong antiferromagnetic coupling between the two metallic ions within paddle-wheel dinuclear copper carboxylates, ferromagnetic orderings are not expected in systems with these building blocks. In fact, the sudden increase in magnetic susceptibility frequently observed at low temperatures is usually ascribed to paramagnetic impurities resulting from the synthetic procedure.⁶² However, more complex magnetic properties have been observed in some coordination polymers containing that type of dimeric entity, including spontaneous magnetization.⁶⁵⁻⁶⁷ Such behavior has been interpreted in terms of a weak ferromagnetic coupling between the dimers or canted antiferromagnetic orderings due to the competition of different intra and interdimeric interactions. But these interpretations are questioned by several authors because of the essentially molecular character of the $\text{Cu}_2(\text{COO})_4$ units in most of these compounds.⁶⁸ Due to strong antiferromagnetic interactions, dimers do not possess at low temperatures a net spin moment that could give rise to weak ferromagnetism or canted ordering. In fact, theoretical calculations by Shen *et al.*⁶⁹ show that the energy barrier necessary to create a net magnetic moment in such dimers would be impossible to overcome at temperatures close to 5 K. These authors have shown that the ferromagnetism observed in certain MOFs with paddle-wheel units linked by conjugated aromatic ligands has its origin in the existence of copper vacancies that allow the existence of localized magnetic moments. The ferromagnetic ordering is achieved via π -electrons of the aromatic linkers that connect the copper-defective dimers. Moreover, it is well known that, in other Cu oxides, Cu or oxygen vacancies produce local moments that enhance ferromagnetism.^{70, 71} According to this model, the presence of a very small number of copper vacancies in the title compound could be the reason why it does not show the weak ferromagnetism described for the isostructural $\text{CsCu}(\text{HCOO})_2\text{Cl}$. It should be noted that vacancies are an inevitable feature of structurally complex systems such as these, but their concentration is strongly influenced by the obtention procedure.

3.6. Electron Paramagnetic Resonance Behavior

The Q-band (300 K) and X-band (300, 175 and 5 K) powder EPR spectra of $\text{RbCu}(\text{HCO}_2)_2\text{Cl}$ are displayed in Figures 6A and 6B, respectively. A set of five broad anisotropic resonances is observed in the Q-band, centered at approximately 480, 650, 925, 1100 and 1380 mT. The X-band displays two intense signals at magnetic fields of approximately 85 and 500 mT, two weaker signals at around 30 and 590 mT, and a weak, complex band at



approximately 315 mT. When the temperature is lowered to 5 K, only the latter can be detected. As is frequently observed for dinuclear copper complexes with carboxylate bridges, the recorded spectra exhibit the expected features of a triplet state ($S=1$) with significant zero-field splitting (ZFS). Therefore, the following spin Hamiltonian (equation (2)), which includes Zeeman electronic and ZFS terms,⁷² has been used to analyze them :

$$\hat{H} = \beta B \mathbf{g} \hat{S} + \hat{S} \mathbf{D} \hat{S} = \beta B \mathbf{g} \hat{S} + D \left(S_z^2 - \frac{2}{3} \right) + E (S_x^2 - S_y^2) \quad (2)$$

where D and E are the axial and rhombic zero field splitting parameters, respectively. As the Zeeman contribution in the X-band experiment is of the same order of magnitude as the ZFS in this type of dimeric entities,⁷³ we used the Q-band spectra to determine the eigen values of the g and D tensors. Adjusting the observed signals by the trial and error method, the following values were obtained: $g_{||} = 2.375$; $g_{\perp} = 2.064$; $|D| = 0.414 \text{ cm}^{-1}$; $|E| < 0.01 \text{ cm}^{-1}$. These parameters were used to simulate the Q-band EPR spectrum, producing the dashed line in Figure 62B, and to identify and label the observed peaks using the standard notation for copper dimers with approximate axial symmetry.⁴² We have also identified the so-called “half-field signal”, which corresponds to the transition between the $M_s = -1$ and $M_s = +1$ states ($\Delta M_s = \pm 2$). This signal is formally forbidden by the EPR spectroscopy selection rule ($\Delta M_s = \pm 1$) and not generated by our simulation program. The calculated g-values are typical of Cu(II) ions in square pyramidal environments with the unpaired electron on the $d_{x^2-y^2}$ orbital. The absolute value of D is at the upper end of the range usually observed for copper carboxylate dimers, as is also the case for other formate compounds.⁷⁴



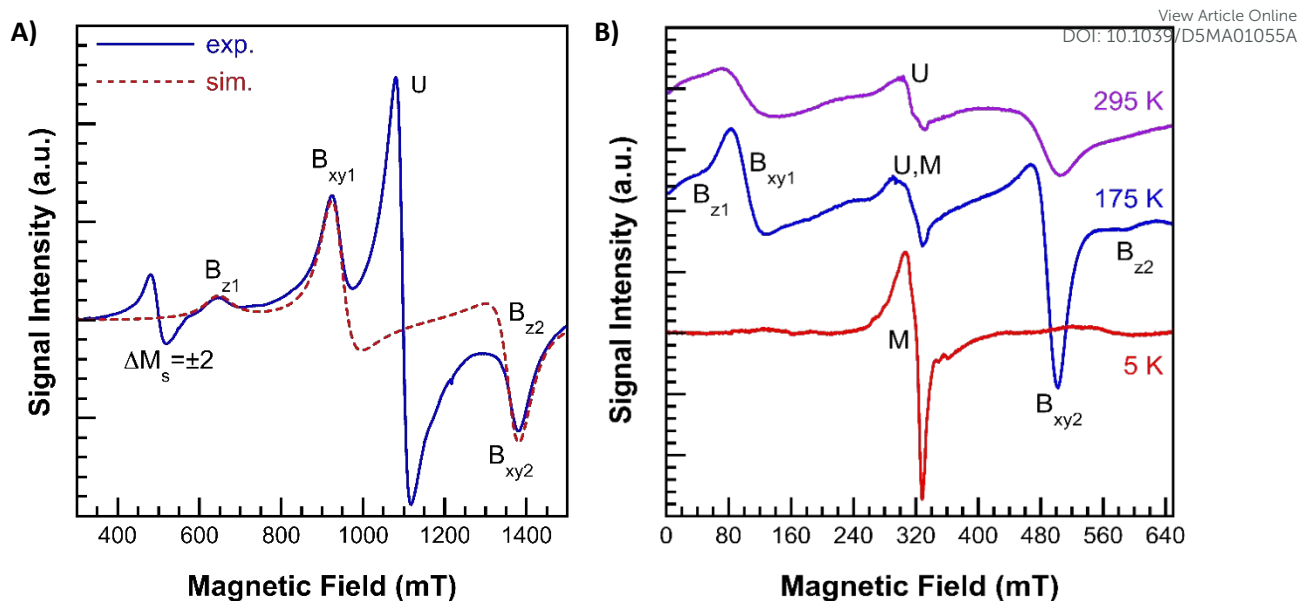


Figure 6. EPR spectra of $\text{RbCu}(\text{HCO}_2)_2\text{Cl}$ powder at (A) 33.9 GHz and 295 K, and (B) 9.4 GHz at 295, 175 and 5 K. Dotted-red line in A is a simulation with the parameters indicated in the text.

The sign of the D parameter cannot be determined using low-frequency EPR or magnetic susceptibility measurements, particularly in strongly antiferromagnetic systems, which become practically EPR-silent at low temperatures. However, we assume that D is negative for this compound since Ozarowski has shown by high-frequency single-crystal EPR studies that this parameter appears to be negative for all binuclear copper carboxylates exhibiting paddle-wheel structures.⁷⁴ The zero-field splitting of the $S=1$ state in these compounds arises from the combined effect of spin dipolar interactions and anisotropic exchange couplings between one electron in the ground state and another one in an excited state. Therefore, the calculated D value can be evaluated as $D = D_{\text{dip}} + D_{\text{ex}}$. Considering that in this type of dimers the Cu---Cu direction practically coincides with the z -axis of the g -tensor, the dipolar contribution can be estimated from the distance between metals (r) using equation (3).⁷⁵

$$D_{\text{dip}} = -\frac{2g_z^2 + (g_x^2 + g_y^2)/2}{2r^3}\beta^2 \quad (3)$$

Using the values of g deduced from the EPR fit and the distance $r_{(\text{Cu} \cdots \text{Cu})} = 2.707 \text{ \AA}$ from the structural resolution, a value of $D_{\text{dip}} = -0.149 \text{ cm}^{-1}$ is obtained from the above expression. Therefore, the exchange contribution to the ZFS is $D_{\text{ex}} = -0.265 \text{ cm}^{-1}$. This value can be used to determine the triplet-singlet separation in dimeric excited states where one cupric ion is in its



electronic ground state ($d_{x^2-y^2}$) while another one is in an excited state (d_{xy} , d_{xz} , d_{yz}).⁷⁶ It is noteworthy that the relationship between D_{ex} and the exchange integral (J) is still unknown, although a correlation between both values has been observed.⁷⁷

The intense line appearing at around 1100 mT in the Q-band spectrum and labeled “U” does not correspond to any of the expected transitions within a triplet $S=1$ state. This signal is too intense to be entirely attributed to the presence of a paramagnetic impurity. Furthermore, its relative intensity decreases with temperature, contrary to what would be expected for such a contribution. Additionally, spectra obtained at various microwave powers suggest that all signals exhibit comparable saturation properties, indicating that they originate from the same magnetic system. Similar resonances have been observed in polymeric structures built on copper dinuclear paddle-wheel units and have been attributed to extended exchange signals originating from the collapse of the fine structure due to interdimeric interactions.⁷⁸⁻⁸¹ Exchange magnetic couplings between spins of neighbouring units can average out the zero-field splitting if they are strong enough. Otherwise, the lines could only collapse for certain crystal orientations. Therefore, spectra recorded in powder samples could show both exchange and molecular resonances. Additionally, interdimeric interactions compete with the strong intradimeric antiferromagnetic couplings characteristics of these compounds. As the population of the excited $S=1$ state rises with rising temperature, the distance between dimers with net spin moment decreases. This leads to a more efficient exchange process between the dimers, which in turn results in an increase in the intensity of the exchange signal “U”, at the expense of the ZFS lines. Considering that the exchange signal is not observable below 100 K in the $RbCu(HCOO)_2Cl$ compound, it can be concluded that the increase in magnetic susceptibility observed at low temperatures is not caused by interdimeric interactions.

Finally, it should be noted that, as the temperature decreases, the relaxation time increases and all the peaks of the spectra become narrower, except for the one corresponding to the extended exchange signal. This improves the resolution of the spectra, even though the intensity of the signals decreases (Figure S4). Below 75 K, the signals corresponding to the triplet state are no longer detectable, confirming the presence of strong intradimeric antiferromagnetic interactions. At 5 K, only the characteristic signal of magnetically isolated Cu(II) ions (labeled “M”) is observed (Figure S5). The hyperfine structure resulting from the interaction of the $S=1/2$ electron spin with the nuclear magnetic moments of the ^{63}Cu and ^{65}Cu



isotopes ($I=3/2$) is partially resolved on the low-field region of the signal. The spin Hamiltonian parameters obtained from the fitting of the powder spectra are: $g_1=2.360$, $g_2=2.111$, $g_3=2.044$, $A_1=0.0140\text{ cm}^{-1}$, $A_2=0.0041\text{ cm}^{-1}$, $A_3<0.0010\text{ cm}^{-1}$. The calculated g-values indicate that these ions are in the same ground state ($d_{x^2-y^2}$) as those forming the dimer, but the environment is notably different in the equatorial plane. EPR signals from mononuclear Cu^{2+} ions in compounds with paddle-wheel units are usually observed and attributed to extra-framework impurities. Nevertheless, it cannot be ruled out that the spectrum is due to the existence of copper vacancies that convert some of the dimers into monomers. In any case, the observed increase in magnetic susceptibility below 70 K (Figure 5) is due to these isolated Cu(II) ions.

3.7. Evaluation of Antibacterial Activity

The antibacterial activity of $\text{RbCu}(\text{HCO}_2)_2\text{Cl}$ was evaluated *in vitro* against two Gram-positive bacteria, *S. aureus* CECT 86 and *L. monocytogenes* CECT 4031, and two Gram-negative bacteria, *E. coli* CECT 99 and *K. pneumoniae* CECT 143^T, using both the disc diffusion and the agar well diffusion methods. For both, 20 μL of a sterile 15 mg/mL solution of compound **1** were used. Table 3 show the values of the inhibition halo diameter from both methods (see Figure S6) and those from the commercial discs of antibiotics used as positive control for each of the bacteria. It is worth noting that the diameters obtained for Gram-positive bacteria were higher than those for Gram-negative in both methods.

Table 3. Mean values ($n=2$) of the diameters of the inhibition halos (mm) obtained in the phenotypic assays using $\text{RbCu}(\text{HCO}_2)_2\text{Cl}$ and commercial antibiotics discs.

	Inhibition halo diameter (mm)			
	Gram-positive bacteria		Gram-negative bacteria	
	<i>S. aureus</i> CECT 86	<i>L. monocytogenes</i> CECT 4031	<i>E. coli</i> CECT 99	<i>K. pneumoniae</i> CECT 143 ^T
Disc diffusion method	12	15	9	8
Agar well diffusion method	25	27	15	15
Norfloxacin (5 μg)	19			
Vancomycin (30 μg)	14.5			
Gentamicin (10 μg)		15		17.5
Ampicillin- sulfactam (10/10 μg)		16		
Trimethoprim-sulfamethoxazole (25 μg)			16	



Nitrofurantoin (300 µg)			18	View Article Online DOI: 10.1039/D5MA01055A
Ciprofloxacin (5 µg)				24.5

Comparison of values from the disc diffusion method with those from the commercial discs of antibiotics displayed the lower antibacterial activity of compound **1** against all the bacteria, except for *L. monocytogenes* CECT 4031, for which the diameters of the halos obtained were similar. The diameters of halos from the agar well diffusion method were, for all the bacteria, greater than those from the disc diffusion method, even though the quantity of compound **1** used was the same. It could be due to a better diffusion of compound in the agar from the wells. Figure 7 shows the results from the quantitative assay to determine the MIC of compound **1**. It is clear that compound **1** was able to inhibit the growth of both Gram-positive and Gram-negative bacteria, though decrease of growth varied with the species and with the concentration. For all the bacteria, except for *S. aureus* CECT 86, the growth was inversely proportional to the concentration of compound **1**, as reported in other studies.⁸² In the case of *S. aureus* CECT 86, the maximum decrease was obtained at a concentration of 800 µg/mL. using larger concentrations did not produce a significant increase in growth inhibition, with values remaining stable around 20 %.



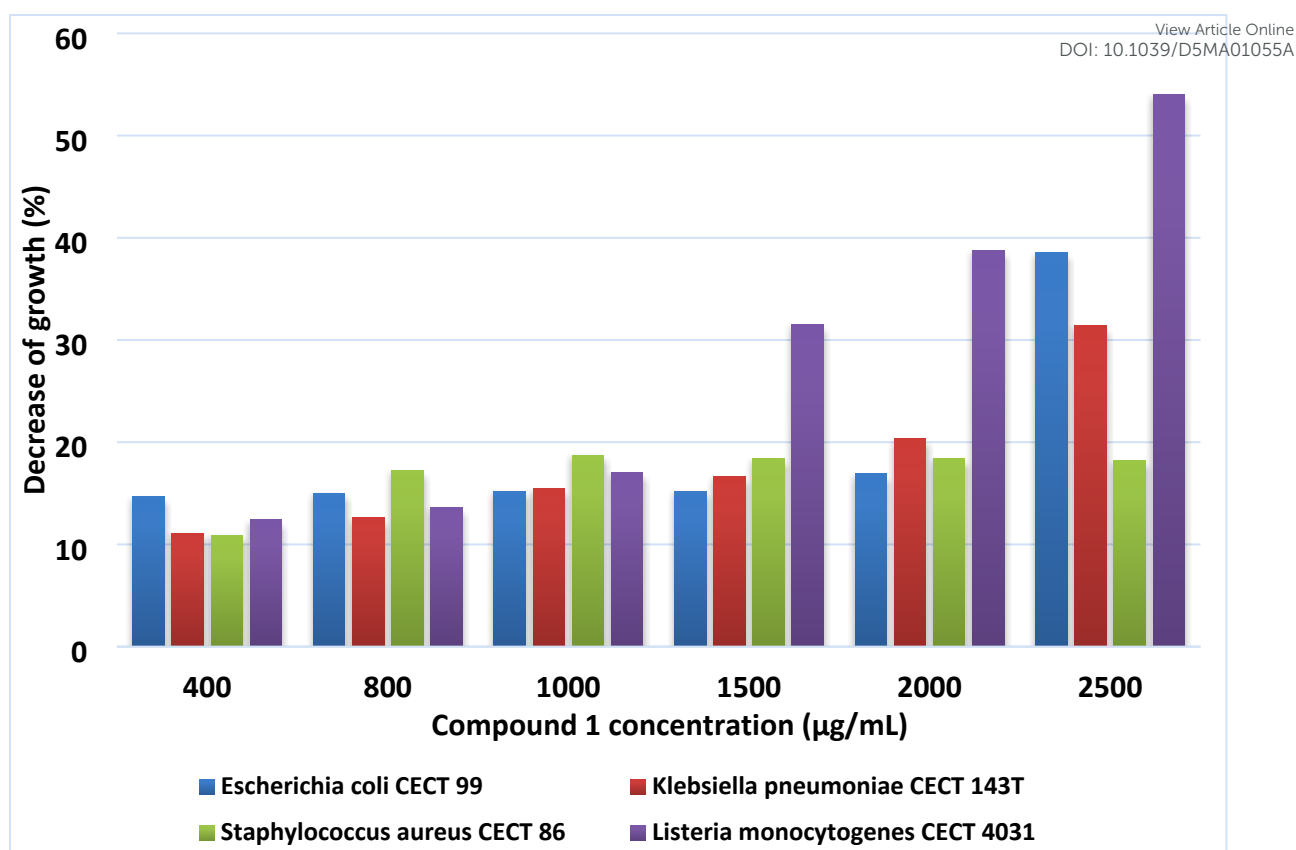


Figure 7. *In vitro* antimicrobial activity of $\text{RbCu}(\text{HCO}_2)_2\text{Cl}$ at different concentrations against two Gram-negative and two Gram-positive bacteria.

The concentrations that were assayed appear to be significantly above the MIC, as the percentages of growth decrease, were less than fifty percent for three of the four bacteria tested. Concentrations above 1000 µg/mL were more effective against *L. monocytogenes* CECT 4031, achieving a growth reduction of 54.02 % at the highest concentration tested, followed by *E. coli* CECT 99 and *K. pneumoniae* CECT 143^T. It might be advisable for future studies to use higher concentrations along with toxicity assessments of compound **1**.

In reference to the measurement of the DO_{600} during the incubation of the strains at different concentrations of compound **1**, it is worthing to note that when *E. coli* CECT 99 was grown in the presence of 2500 µg/mL of compound **1**, the DO_{600} remained constant during the 24 h of incubation and the counts of viable cells at the end of incubation showed that the cells from the inoculum had remained alive without showing growth. This observation suggests that compound **1** at this concentration has a bacteriostatic effect. A similar result was observed for *L. monocytogenes* CECT 4031 at concentrations of 2000 and 2500 µg/mL.



With respect to the antibacterial activity of the copper compounds, some authors reported that it depends on the geometry of the complexes and the nature of the ligands, because both factors influence the lipophilic character of the compounds, affecting their permeability through the cytoplasmic membrane.^{83, 84} The mechanism of action described for these compounds are diverse although in many respects still unknown.⁸⁵ For example, it has been suggested that the release of copper ions causes the inactivation of enzymes,⁸⁶ and more recently that the metallic chelates of Cu^{2+} act disturbing the microbial metabolism and producing their destruction.⁷³ Other possible mechanisms include damage to DNA by reactive oxygen species (ROS) produced through Fenton-type reactions, as well as a decrease in cell membrane integrity.^{20, 27} Differences observed in the activity against Gram-positive and Gram-negative bacteria may stem from variations in the structure and chemical composition of their cell walls, as noted for other metallic compounds.⁸⁷

The antibacterial activity of metal-based complexes can be rationalized using chelation theory and Tweedie's polarization model.^{26, 88-92} Typically, the chelation modifies metal ion properties, enhancing membrane penetration and polarization-induced reactive oxygen species (ROS) generation, which together account for the superior antibacterial activity of metal complexes.²⁶ For the present compound, the antibacterial activity arises from synergistic structural and electronic effects. We suggest that chelation of Cu(II) by bridging formate ligands delocalizes the positive charge over oxygen atoms, reducing the metal center's polarity and enhancing its lipophilicity relative to the hydrated Cu^{2+} ion. This favours interaction with bacterial surfaces and membrane penetration. According to Tweedie's model, the Cu -formate environment also promotes polarization of negatively charged bacterial membranes, facilitating copper uptake.⁸⁸ Additionally, the distorted Cu^{2+} sites may undergo $\text{Cu}^{2+}/\text{Cu}^{+}$ redox cycling, generating ROS that damage key biomolecules.²⁶

4. Conclusion

To conclude, a new copper (II)-based MOF paddle-wheel-like compound, $\text{RbCu}(\text{HCO}_2)_2\text{Cl}$, was successfully synthesized and characterized using spectroscopic, thermal, and magnetic techniques. Single-crystal X-ray diffraction revealed that MOF **1** crystallizes in a monoclinic system with a 3D framework built from dinuclear Cu(II) paddle-wheel units, where each Cu(II) center adopts a square-pyramidal geometry with a $\text{Cu}\cdots\text{Cu}$ distance of 2.7070(7)



Å. The Rb⁺ cations serve as counter-ions, ensuring charge balance within the framework. The thermal stability of compound **1** was studied. Upon further heating of compound **1**, its resulting residue corresponds to binary (RbCl) and metallic Cu species. Magnetic studies revealed strong intradimer antiferromagnetic exchange coupling ($J = -531 \text{ cm}^{-1}$) between Cu²⁺ centers, corroborated by EPR spectra showing characteristic triplet-state ($S = 1$) features with zero-field splitting. The in vitro antibacterial tests against *S. aureus*, *L. monocytogenes*, *E. coli*, and *K. pneumoniae* demonstrated both bacteriostatic and bactericidal activity, suggesting its potential as a promising antimicrobial agent. Overall, these findings highlight the multifunctional nature of this Cu(II)-based paddle-wheel MOF, encouraging further investigation into its magnetic behavior and the development of related bioactive coordination materials for potential biological applications.

Authors contribution

Asmae Ben Abdelhadi: writing-original draft, methodology, investigation, formal analysis. Safaa Hidaoui: methodology, formal analysis. Rachid Ouarsal: writing-review & editing, validation, methodology, formal analysis. Morgane Poupon: software, formal analysis. Michal Dusek: software, formal analysis. María de los Llanos Palop Herreros: writing original draft, validation, methodology, formal analysis. Marco Antonio López de la Torre: methodology, investigation, formal analysis. Luis Lezama: writing original draft, validation, methodology, investigation, formal analysis. Brahim El Bali: conceptualization, validation, formal analysis, writing-review & editing. Mohammed Lachkar: supervision, project administration, resources, writing-review & editing. Abderrazzak Douhal: supervision, project administration, resources, writing-review & editing. All authors read and approved the manuscript.

Conflicts of interest

There are no conflicts of interest to declare.

Data availability

The data supporting this article have been included as part of the Supplementary Information.



Crystallographic data for compound **1** has been deposited at the Cambridge Crystallographic Data Centre (CCDC) under CCDC 2468965 and can be obtained from www.ccdc.cam.ac.uk/data_request/cif (CCDC 2468965).

Acknowledgements

This work was supported by the following grants: grant PID2020-116519RB-I00 and TED2021-131650B-I00 funded by MICIU/AEI/10.13039/501100011033 and the European Union (EU). A.B.A. is grateful for the grant from the Spanish Service for the Internationalization of Education (SEPIE), through the EU Erasmus+ key action program (2020-1-ES01-KA107-079868). The authors A. B. A., S. H., R. O., B. E. B. and M. L. would like to acknowledge the technical assistance of the Interface Regional University Center (University Sidi Mohammed Ben Abdellah, Fez, Morocco). Crystallographic analysis was supported by the project 20-LM2023051 of the Czech Nanolab Infrastructures, supported by MEYS CR.

References

1. J. Annamalai, P. Murugan, D. Ganapathy, D. Nallaswamy, R. Atchudan, S. Arya, A. Khosla, S. Barathi and A. K. Sundramoorthy, *Chemosphere*, 2022, **298**, 134184.
2. Q. Zhang, S. Yan, X. Yan and Y. Lv, *Sci. Total Environ.*, 2023, **902**, 165944.
3. D. Li, A. Yadav, H. Zhou, K. Roy, P. Thanasekaran and C. Lee, *Global Challenges*, 2024, **8**, 2300244.
4. L. Jiao, Y. Wang, H.-L. Jiang and Q. Xu, *Advanced Materials*, 2018, **30**, 1703663.
5. B. Pato-Doldán, L. C. Gómez-Aguirre, J. M. Bermúdez-García, M. Sánchez-Andújar, A. Fondado, J. Mira, S. Castro-García and M. A. Señarís-Rodríguez, *RSC Advances*, 2013, **3**, 22404-22411.
6. J. Wang, X.-L. Xu and X. a. Li, *Advanced Materials Interfaces*, 2023, **10**, 2300123.
7. Z. Wang, K. Hu, S. Gao and H. Kobayashi, *Advanced Materials*, 2010, **22**, 1526-1533.
8. Y. Wang, R. Cao, W. Bi, X. Li, D. Yuan and D. Sun, *Microporous and Mesoporous Materials*, 2006, **91**, 215-220.
9. P. Kar, R. Biswas, M. G. B. Drew, Y. Ida, T. Ishida and A. Ghosh, *Dalton Transactions*, 2011, **40**, 3295-3304.
10. L. C. Gómez-Aguirre, B. Pato-Doldán, J. Mira, S. Castro-García, M. A. Señarís-Rodríguez, M. Sánchez-Andújar, J. Singleton and V. S. Zapf, *Journal of the American Chemical Society*, 2016, **138**, 1122-1125.
11. Z. Zhang, H. Yu, X. Shen, L. Sun, S. Yue and H. Tang, *Materials*, 2021, **14**.
12. M. Mączka, A. Gągor, M. Ptak, W. Paraguassu, T. A. da Silva, A. Sieradzki and A. Pikul, *Chemistry of Materials*, 2017, **29**, 2264-2275.
13. A. B. Abdelhadi, R. Ouarsal, M. Poupon, M. Dusek, J. P. A. González, L. Lezama, B. El Bali, M. Lachkar and A. Douhal, *Materials Advances*, 2024, **5**, 6154-6161.
14. M. Mendt, M. Maliuta, S. Ehrling, F. Schwotzer, I. Senkovska, S. Kaskel and A. Pöpl, *The Journal of Physical Chemistry C*, 2022, **126**, 625-633.
15. N. Ahmad, H. A. Younus, A. H. Chughtai, K. Van Hecke, Z. A. Khattak, Z. Gaoke, M. Danish and F. Verpoort, *Catalysis Science & Technology*, 2018, **8**, 4010-4017.



16. T. Zanette, Y. M. Variani, B. P. Nicola, S. Gutiérrez-Tarriño, C. Cerezo-Navarrete, G. Agostini, P. Oña-Burgos, C. W. Lopes and K. Bernardo-Gusmão, *Catalysis Today*, 2025, **444**, 114988. View Article Online
DOI: 10.1039/D5MA01055A
17. T.-R. Lin, C.-H. Lee, Y.-C. Lan, S. Mendiratta, L.-L. Lai, J.-Y. Wu, K.-M. Chi and K.-L. Lu, *Polymers*, 2018, **10**, 1398.
18. Z. Zhang, H. Yu, X. Shen, L. Sun, S. Yue and H. Tang, *Materials*, 2021, **14**, 3125.
19. M.-H. Yan, J. Wang, X.-Y. Su, H. Sakiyama, N. Qi, M. Afzal, A. Alarifi, D. Srivastava and A. Kumar, *New Journal of Chemistry*, 2023, **47**, 11134-11142.
20. A. L. Pereira, M. A. Vasconcelos, A. L. Andrade, I. M. Martins, A. K. Holanda, A. C. Gondim, D. P. Penha, K. L. Bruno, F. O. Silva and E. H. Teixeira, *Current Microbiology*, 2023, **80**, 133.
21. Viola, N. Muhammad, A. Noor, M. Sirajuddin, M. Kubicki, S. Rahim, A. Samad, S. Shujah, A. Wadood and S. Ali, *Pharmaceuticals*, 2023, **16**, 1462.
22. F. Li, K. Liu, S. Fan, T. Qin, S. Xiong and J. Wang, *Zeitschrift für anorganische und allgemeine Chemie*, 2018, **644**, 560-563.
23. V. Paredes-García, R. C. Santana, R. Madrid, A. Vega, E. Spodine and D. Venegas-Yazigi, *Inorganic Chemistry*, 2013, **52**, 8369-8377.
24. K. Ngece, V. Khwaza, A. M. Paca and B. A. Aderibigbe, *Antibiotics*, 2025, **14**, 516.
25. M. Premkumar, D. Kaleeswaran, G. Kaviyaran, D. Prasanth and G. Venkatachalam, *ChemistrySelect*, 2019, **4**, 7507-7511.
26. M. S. Alhussaini, A. A. I. Alyahya and A. A. Al-Ghanayem, *Dyes and Pigments*, 2025, **243**, 113040.
27. B. Sharma, S. Shukla, R. Rattan, M. Fatima, M. Goel, M. Bhat, S. Dutta, R. K. Ranjan and M. Sharma, *International Journal of Biomaterials*, 2022, **2022**, 6819080.
28. V. J. Tamilpriyai, P. Nagarasu, K. S. Dharshini, P. Dhanaraj, A. Veerappan, D. Moon, S. P. Anthony and V. Madhu, *Journal of Molecular Structure*, 2023, **1294**, 136414.
29. D. Majumdar, S. Roy, J. Elizabeth Philip, B. Tüzün and S. Hazra, *Inorganic Chemistry Communications*, 2024, **160**, 111933.
30. S. Notz, K. Müller, R. Thomas, T. Rüffer and H. Lang, *Inorganic Chemistry Communications*, 2024, **167**, 112765.
31. P. Edelsbacher, G. Redhammer and U. Monkowius, *Monatshefte für Chemie-Chemical Monthly*, 2020, **151**, 543-547.
32. B. Saha, M. Bhattacharjee, S. R. Boruah, R. D. Purkayastha, R. M. Gomila, S. Chowdhury, A. Mandal and A. Frontera, *Journal of Molecular Structure*, 2023, **1272**, 134104.
33. O. Rojas, G. Mirzoyan, Z. Adamyan, V. V. Papoyan, G. Amatuni and N. Ananikian, *Scientific Reports*, 2025, **15**, 11758.
34. M. Barwiolek, D. Jankowska, A. Kaczmarek-Kędziera, I. Lakomska, J. Kobylarczyk, R. Podgajny, P. Popielarski, J. Masternak, M. Witwicki and T. M. Muzioł, *International Journal of Molecular Sciences*, 2023, **24**, 3017.
35. J. Soldevila-Sanmartín, J. A. Ayllón, T. Calvet, M. Font-Bardia, C. Domingo and J. Pons, *Inorganic Chemistry Communications*, 2016, **71**, 90-93.
36. J. Zhou, L. Du, Z. Li, Y. Qiao, J. Liu, M. Zhu, P. Chen and Q. Zhao, *Journal of Coordination Chemistry*, 2013, **66**, 2166-2177.
37. H. Phetmung and A. Nucharoen, *Polyhedron*, 2019, **173**, 114121.
38. E. Y. Bivián-Castro, M. Flores-Alamo, R. Escudero, V. Gómez-Vidal, J. J. N. Segoviano-Garfias, J. Castañeda-Contreras and Q. E. Saavedra-Arroyo, *Materials*, 2023, **16**, 4866.
39. Viola, N. Muhammad, M. Ikram, S. Rehman, S. Ali, M. N. Akhtar, M. A. AlDamen and C. Schulzke, *Journal of Molecular Structure*, 2019, **1196**, 754-759.
40. B. Rafique, K. Shafique, S. Hamid, S. Kalsoom, M. Hashim, B. Mirza, L. Jafri and M. Iqbal, *Journal of Biomolecular Structure and Dynamics*, 2022, **40**, 5446-5461.
41. M. Iqbal, S. Ali, Z.-U. Rehman, N. Muhammad, M. Sohail and V. Pandarinathan, *Journal of Coordination Chemistry*, 2014, **67**, 1731-1745.
42. J. A. Weil and J. R. Bolton, *Electron paramagnetic resonance: elementary theory and practical applications*, John Wiley & Sons, 2007.



43. C. Sarkar, A. Majumder, I. Das, S. Maji, J. Kłak, G. Vijaykumar, S. Mandal and M. Bera, *Journal of Molecular Structure*, 2024, **1318**, 139423. View Article Online
DOI: 10.1039/D5MA01055A
44. S. M. Bovill and P. J. Saines, *CrystEngComm*, 2015, **17**, 8319-8326.
45. L. Palatinus and G. Chapuis, *J. Appl. Cryst.*, 2007, **40**, 786-790.
46. V. Petříček, L. Palatinus, J. Plášil and M. Dušek, *Z Kristallogr Cryst Mater*, 2023, **238**, 271-282.
47. K. Brandenburg and H. Putz, *Crystal Impact GbR, Bonn, Germany*, 2006.
48. H. Fleming, J. Etchells and R. Costilow, *Applied microbiology*, 1975, **30**, 1040-1042.
49. S. Magaldi, S. Mata-Essayag, C. H. De Capriles, C. Pérez, M. Colella, C. Olaizola and Y. Ontiveros, *International journal of infectious diseases*, 2004, **8**, 39-45.
50. J. Zhou, S. Jin, R. Sun, C. Chai, M. Hao, X. Zhong and X. Chen, *Physical Review Materials*, 2021, **5**, 074405.
51. K. Karthik and A. M. Qadir, *Journal of Structural Chemistry*, 2019, **60**, 1126-1132.
52. B. Saha, M. Bhattacharjee, S. R. Boruah, R. N Dutta Purkayastha, R. M Gomila, S. Chowdhury, A. Mandal and A. Frontera, *Journal of Molecular Structure*, 2023, **1272**, 134104.
53. M. Trzebiatowska-Gusowska and A. Gągor, *Journal of Coordination Chemistry*, 2017, **70**, 1-22.
54. C. W. A. Paschoal, M. R. Moura, A. P. Ayala, J. M. Sasaki, P. T. C. Freire, F. E. A. Melo, J. Mendes Filho, I. Guedes, A. G. Leyva, G. Polla, D. Vega and P. K. Perazzo, *Journal of Solid State Chemistry*, 2000, **154**, 338-343.
55. M. A. Moreno, O. Gálvez, B. Maté, V. J. Herrero and R. Escribano, *The Journal of Physical Chemistry A*, 2011, **115**, 70-75.
56. A. Ciupa and M. Ptak, *Vibrational Spectroscopy*, 2016, **86**, 67-74.
57. M. Mączka, A. Ciupa, A. Gągor, A. Sieradzki, A. Pikul and M. Ptak, *Journal of Materials Chemistry C*, 2016, **4**, 1186-1193.
58. A. P. Ayala, J. M. Henriques Neto, C. W. A. Paschoal, I. Guedes, J. M. Sasaki, P. T. C. Freire, F. E. A. Melo, J. Mendes Filho, A. G. Leyva, G. Polla, D. Vega and P. K. Perazzo, *Journal of Raman Spectroscopy*, 2000, **31**, 491-495.
59. Y. Abusa, J. Greenfield, G. Viswanathan, S. Goswami, E. Ross, P. Yox, R. Oppong, I. Ojo, J. Liu, A. Ozarowski and K. Kovnir, *Chemical Science*, 2025, **16**, 11027-11038.
60. E. Eikeland, N. Lock, M. Filsø, M. Stingaciu, Y. Shen, J. Overgaard and B. B. Iversen, *Inorganic Chemistry*, 2014, **53**, 10178-10188.
61. B. Bleaney and K. Bowers, *Proceedings of the Royal Society of London. Series A. Mathematical and Physical Sciences*, 1952, **214**, 451-465.
62. O. Kahn, *Publishers Inc., New York*, 1993, 167-174.
63. A. Rodríguez-Forte, P. Alemany, S. Alvarez and E. Ruiz, *Chemistry—A European Journal*, 2001, **7**, 627-637.
64. R. L. Carlin, *Magnetochemistry*, Springer Science & Business Media, 2012.
65. S. S.-Y. Chui, S. M.-F. Lo, J. P. Charmant, A. G. Orpen and I. D. Williams, *Science*, 1999, **283**, 1148-1150.
66. B. Moulton, J. Lu, R. Hajndl, S. Hariharan and M. J. Zaworotko, *Angewandte Chemie*, 2002, **114**, 2945-2948.
67. S. Feng, H. Duan, H. Tan, F. Hu, C. Liu, Y. Wang, Z. Li, L. Cai, Y. Cao, C. Wang, Z. Qi, L. Song, X. Liu, Z. Sun and W. Yan, *Nature Communications*, 2023, **14**, 7063.
68. D. MasPOCH, D. Ruiz-Molina and J. Veciana, *Chemical Society Reviews*, 2007, **36**, 770-818.
69. L. Shen, S.-W. Yang, S. Xiang, T. Liu, B. Zhao, M.-F. Ng, J. r. Göettlicher, J. Yi, S. Li and L. Wang, *Journal of the American Chemical Society*, 2012, **134**, 17286-17290.
70. S. Shi, D. Gao, Q. Xu, Z. Yang and D. Xue, *CrystEngComm*, 2015, **17**, 2118-2122.
71. D. Gao, J. Zhang, J. Zhu, J. Qi, Z. Zhang, W. Sui, H. Shi and D. Xue, *Nanoscale research letters*, 2010, **5**, 769.
72. E. Wasserman, L. C. Snyder and W. A. Yager, *The Journal of Chemical Physics*, 1964, **41**, 1763-1772.
73. W. R. Hagen, *International Journal of Molecular Sciences*, 2023, **24**, 14793.
74. A. Ozarowski, *Inorganic chemistry*, 2008, **47**, 9760-9762.



75. A. Bencini and D. Gatteschi, *Electron paramagnetic resonance of exchange coupled systems*, Springer Science & Business Media, 2012.
76. P. K. Ross, M. D. Allendorf and E. I. Solomon, *Journal of the American Chemical Society*, 1989, **111**, 4009-4021.
77. L. Gutierrez, G. Alzuet, J. Borrás, A. Castineiras, A. Rodríguez-Forteza and E. Ruiz, *Inorganic Chemistry*, 2001, **40**, 3089-3096.
78. M. Perec, R. Baggio, R. P. Sartoris, R. C. Santana, O. Peña and R. Calvo, *Inorganic chemistry*, 2010, **49**, 695-703.
79. M. Simenas, M. Kobalz, M. Mendt, P. Eckold, H. Krautscheid, J. r. Banys and A. Pöppl, *The Journal of Physical Chemistry C*, 2015, **119**, 4898-4907.
80. V. Paredes-García, R. C. Santana, R. Madrid, A. s. Vega, E. Spodine and D. Venegas-Yazigi, *Inorganic Chemistry*, 2013, **52**, 8369-8377.
81. A. Pöppl, S. Kunz, D. Himsl and M. Hartmann, *The Journal of Physical Chemistry C*, 2008, **112**, 2678-2684.
82. S. Reja, D. Sarkar, K. Sarkar, D. Mukherjee, T. Fayaz, P. Sanphui and R. K. Das, *Inorganica Chimica Acta*, 2024, **560**, 121809.
83. G. Borthagaray, M. Mondelli and M. Torre, *J. Infect. Dis. Epidemiol*, 2016, **2**, 10.23937.
84. S. K. Nandanwar and H. J. Kim, *ChemistrySelect*, 2019, **4**, 1706-1721.
85. A. C. Hangan, R. L. Lucaciu, A. Turza, L. Dican, B. Sevastre, E. Páll, L. S. Oprean and G. Borodi, *International Journal of Molecular Sciences*, 2023, **24**, 13819.
86. J. A. Lemire, J. J. Harrison and R. J. Turner, *Nature Reviews Microbiology*, 2013, **11**, 371-384.
87. A. B. Abdelhadi, S. Rodríguez-Sánchez, R. Ouarsal, M. Saadi, L. El Ammari, N. Morley, B. El Bali, Ó. Gómez-Torres, M. Lachkar and A. Douhal, *Materials Advances*, 2024, **5**, 3058-3066.
88. T. BG., *Phytopathology*, 1964, **55**, 910-918.
89. C. Barbot, L. Gouriou, M. Mignot, M. Sebban, P. Zhang, D. Landy, C.-C. Ling and G. Gouhier, *Molecules*, 2025, **30**, 3263.
90. S. Arulmozhi, G. Sasikumar, A. Subramani, M. K. Mohammed, S. J. A. Ali, S. Ponnusamy, M. S. Jabir, A. M. Elgorban, W. Zhang and H. Natarajan, *ACS omega*, 2023, **8**, 34458-34470.
91. D. Majumdar, J. E. Philip, S. Roy, B. Gassoumi and H. Ghalla, *BMC chemistry*, 2025, **19**, 227.
92. S. S. A. Fathima, M. M. S. Meeran and E. Nagarajan, *Structural Chemistry*, 2020, **31**, 521-539.

View Article Online
DOI: 10.1039/D5MA01055A



Data availability statement

View Article Online
DOI: 10.1039/D5MA01055A

The data supporting this article have been included as part of the Supplementary Information.

Crystallographic data for compound **1** has been deposited at the Cambridge Crystallographic Data Centre (CCDC) under CCDC 2468965 and can be obtained from www.ccdc.cam.ac.uk/data_request/cif (CCDC 2468965).

